



# Pressure and Temperature Dependence of the Hydrogen Oxidation and Evolution Reaction Kinetics on Pt Electrocatalysts via PEMFC-based Hydrogen-Pump Measurements

Björn M. Stühmeier,<sup>\*,\*z</sup> Markus R. Pietsch,<sup>=</sup> Jan N. Schwämmlein,<sup>\*</sup>  and Hubert A. Gasteiger<sup>\*\*</sup>

Chair of Technical Electrochemistry, Department of Chemistry and Catalysis Research Center, Technical University of Munich, D-85748 Garching, Germany

The hydrogen oxidation and evolution reaction (HOR/HER) has been widely investigated due to its importance for a broad variety of applications especially in electrolysis and fuel cells. However, owing to its extremely fast kinetics, kinetic data can only be obtained with experimental setups that provide very fast mass transport, so that the effect of hydrogen partial pressure ( $p_{\text{H}_2}$ ) and kinetic limitations at high overpotentials are not yet fully understood. Here we report detailed kinetic investigations on the temperature and pressure dependence of the HOR/HER kinetics on carbon supported platinum (Pt/C) using the PEMFC-based  $\text{H}_2$ -pump approach. By using ultra-low platinum loadings, we could show that the apparent activation energy of the HOR/HER on platinum increases with increasing  $p_{\text{H}_2}$ , due to a diminishing effect of the hydrogen adsorption enthalpy with increasing coverage by adsorbed hydrogen atoms on the Pt surface. Consequently, the HOR/HER reaction order with respect to  $p_{\text{H}_2}$  also depends on the temperature. We further observed that the HOR reaches a limiting current at high HOR overpotentials that showed a direct proportionality to  $p_{\text{H}_2}$  and a pressure-independent activation energy. We ascribe this to a limitation of the hydrogen adsorption rate either by a rate limiting Tafel-reaction or mass transport limitations.

© 2021 The Author(s). Published on behalf of The Electrochemical Society by IOP Publishing Limited. This is an open access article distributed under the terms of the Creative Commons Attribution 4.0 License (CC BY, <http://creativecommons.org/licenses/by/4.0/>), which permits unrestricted reuse of the work in any medium, provided the original work is properly cited. [DOI: 10.1149/1945-7111/ac099c]



Manuscript submitted April 16, 2021; revised manuscript received June 2, 2021. Published June 23, 2021. This was paper 2337 presented during PRiME 2020, October 4–9, 2020.

Supplementary material for this article is available [online](#)

One of the main challenges of the transition to renewable energies is the development of efficient energy storage technologies at relatively low costs. Here, water electrolyzers (ELs) and hydrogen fuel cells (FCs) play a central role for the use of  $\text{H}_2$  as chemical energy storage.<sup>1–3</sup> The main performance limitation in both systems are the sluggish reactions at the oxygen electrode, i.e., the oxygen evolution reaction (OER) for electrolyzers and the oxygen reduction reaction (ORR) for fuel cells. This is especially the case for acidic systems based on proton exchange membranes (PEMs), where the hydrogen evolution reaction (HER) on the cathode of a PEMEL and the hydrogen oxidation reaction (HOR) on the anode of a PEMFC according to Eq. 1 are extremely fast.<sup>4–6</sup>

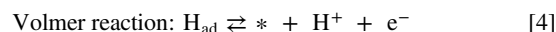
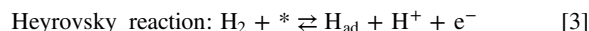
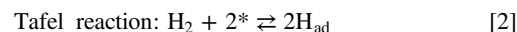


Consequently, only small amounts of Pt ( $\approx 0.025$ – $0.05 \text{ mg}_{\text{Pt}} \text{ cm}_{\text{geo}}^{-2}$ ) are required to limit the HOR/HER voltage loss contribution to only a few mV.<sup>1,6,7</sup> At such low Pt loadings, however, even a modest loss of electrochemically active surface area (ECSA) of the hydrogen catalysts due to cell-reversal and start-up and shut-down events can lead to a noticeable performance degradation.<sup>8,9</sup> Although the occurrence of these events can be reduced by system mitigation strategies,<sup>10,11</sup> a better understanding of the HOR/HER kinetics is essential for accurate durability predictions and the development of next generation system designs.

While the HOR/HER reaction rates on platinum and platinum alloy catalysts in alkaline environment can be determined precisely with rotating ring disk (RDE) measurements,<sup>12–14</sup> this is not possible at low pH due to the two orders of magnitude higher reaction rates that by far exceed the slow mass transport limited currents afforded by the RDE configuration.<sup>15–17</sup> In recent years, new experimental approaches have been developed, which allow for fast transport of hydrogen to the catalyst, thereby enabling kinetic investigations at

low pH as well.<sup>4,5,15,17–22</sup> Although a change in the hydrogen binding energy (HBE) could therefore be identified as one reason for the decrease in HOR/HER activity with pH,<sup>14,23</sup> these studies have highlighted an overall lack of fundamental understanding at the mechanistic level of the HOR/HER, especially at high overpotentials.

From a mechanistic point of view, Eq. 1 can be divided in a series of two of the following elementary steps, where a surface adsorption site (\*) is required for hydrogen adsorption:<sup>24</sup>



In order to unveil the overall reaction mechanism, it is necessary to determine the electrochemical reaction parameters, i.e., the exchange current density  $i_0$  (in  $\text{A cm}_{\text{Pt}}^{-2}$ ), its activation energy  $E_{\text{A}}$  (in  $\text{kJ mol}^{-1}$ ), the anodic and cathodic transfer coefficients  $\alpha_{\text{a/c}}$  or the Tafel slopes in  $\text{mV decade}^{-1}$ , respectively, and the reaction order with regards to the hydrogen partial pressure. Knowing these parameters would allow to determine which set of the above listed reactions establish the HOR/HER equilibrium, which of these reactions constitutes the rate determining step (RDS), and how the reaction mechanism might change with overpotential.<sup>24,25</sup>

Many studies in the literature have shown that close to the equilibrium potential, the HOR/HER kinetics can be described by the Butler-Volmer equation,<sup>4,13,15,17,21,26,27</sup> which therefore is commonly used to describe the potential dependence of the HOR/HER kinetics:<sup>24,28</sup>

$$\text{Butler – Volmer kinetics: } i_{\text{spec}} = i_0 \left( e^{\frac{\alpha_{\text{a}} F \eta}{RT}} - e^{-\frac{\alpha_{\text{c}} F \eta}{RT}} \right) \quad [5]$$

with  $i_{\text{spec}}$  being the Pt surface specific current density (in  $\text{A cm}_{\text{Pt}}^{-2}$ ),  $i_0$  the exchange current density (in  $\text{A cm}_{\text{Pt}}^{-2}$ ),  $\alpha_{\text{a/c}}$  the anodic/cathodic transfer coefficients,  $\eta$  the overpotential (in V), i.e., the difference between the electrode potential and the equilibrium

<sup>†</sup>These authors contributed equally to this work.

\*Electrochemical Society Student Member.

\*\*Electrochemical Society Fellow.

<sup>z</sup>E-mail: [bjorn.stuehmeier@tum.de](mailto:bjorn.stuehmeier@tum.de)

potential,  $F$  the Faraday constant ( $96,484 \text{ A s mol}^{-1}$ ),  $R$  the universal gas constant ( $8.314 \text{ kJ mol}^{-1} \text{ K}^{-1}$ ), and  $T$  the temperature (in K). To a first approximation, a Tafel-Volmer (TV) reaction pathway with a rate determining Volmer-step would result in a sum of the anodic and cathodic transfer coefficients of one ( $\alpha_a + \alpha_c = 1$ ), while the Heyrovsky-Volmer (HV) mechanism would yield  $\alpha_a + \alpha_c = 2$  (independent on whether Volmer or Heyrovsky are the RDS, as long as the RDS is the same for the forward and backward reaction).<sup>29,30</sup> However, a more rigorous analysis of the HV mechanism shows that it does not strictly follow Butler-Volmer kinetics. Instead, the sum of transfer coefficients changes from two to unity at higher overpotentials with the exact occurrence of this transition strongly depending on the equilibrium hydrogen coverage of the catalyst and the relative rates of the elementary steps, so that the initial state might not even be observed.<sup>25,28</sup>

While the HOR/HER mechanism has been excessively investigated for decades, many older and even some recent studies on the predominant mechanism of the HOR/HER in acid have erroneously relied on kinetic parameters from RDE measurements,<sup>31–37</sup> which have been shown to be mainly affected by  $\text{H}_2$  mass transport rates.<sup>15,16,22</sup> The validity of these earlier studies regarding a mechanistic understanding is therefore to be questioned. Most commonly, HOR/HER kinetic studies based on experimental approaches that allow for fast mass transport, a TV (Tafel-Volmer) mechanism was used for the description of the HOR/HER kinetics,<sup>4,14,15,17,18,23,38</sup> while a predominant HV (Heyrovsky-Volmer) mechanism was proposed by Zalitis et al.<sup>5</sup> With increasing overpotentials, however, the HOR/HER currents have been reported to deviate from the Butler-Volmer behavior and to reach a limiting current even under experimental conditions that allow for fast mass transport; in these cases, the appearance of a limiting current has been explained by a transition from a TV to a HV mechanism at high anodic overpotentials,<sup>25,39</sup> by a transition to a rate determining Tafel-step,<sup>15,18,38</sup> or by active site blocking.<sup>20</sup>

In this study, we report detailed kinetic investigations on the temperature and pressure dependence of the HOR/HER kinetics on a Pt/C catalyst using the  $\text{H}_2$ -pump approach. After discussing the observed differences in the measured HOR/HER currents between a dynamic measurement approach (i.e., cyclic voltammetric scans), and a static measurement approach (i.e., galvanostatic or potentiostatic conditions),  $i_0$ -values are extracted for a broad matrix of temperatures and  $\text{H}_2$  partial pressures in order to determine the  $\text{H}_2$  partial pressure ( $p_{\text{H}_2}$ ) dependent activation energies and the temperature dependent reaction orders with respect to  $p_{\text{H}_2}$ . These findings will be critically discussed with respect to the underlying reaction mechanism and the involved elementary steps. Furthermore, the extensive set of data will be used for a detailed investigation of the limiting current for the HOR at high overpotentials. Thus, the activation energy and the pressure dependence of this limiting current will be determined, followed by a critical discussion of the implications to the reaction mechanism or possible mass transport limitations.

## Experimental

**Hardware and experimental setup.**—All hydrogen-pump measurements were performed on a customized G60 test station (Greenlight Innovation Corp., USA) modified to feature pure  $\text{H}_2$  instead of air/ $\text{O}_2$  on the cathode side; the normally present connection to a CO containing gas line for CO stripping analysis was removed in order to eliminate the risk of unintended CO poisoning (CO stripping analysis was thus conducted on a different test station). The current range of the potentiostat (Reference 3000, Gamry Instruments, USA) was extended by a booster (Reference 30 K Booster, Gamry Instruments, USA). All measurements were carried out with a  $5 \text{ cm}^2$  active area single-cell hardware, using commercial graphite flow fields (7 parallel channels, one serpentine, 0.5 mm lands/channels; manufactured by Poco Graphite, Entegris GmbH, Germany, according to our design<sup>40</sup>). Gas diffusion layers

(GDLs) were the same in all experiments (H14C10, Freudenberg KG, Germany) and the GDL compression was adjusted to  $13 \pm 0.5\%$  by quasi-incompressible, PTFE-coated fiberglass gaskets (Fiberflon, Fiberflon GmbH & Co. KG, Germany), assembled at a torque of 12 Nm resulting in a contact pressure of  $\approx 1.5 \text{ MPa}$  on the active area (for details see Simon et al.<sup>41</sup>).

**Membrane electrode assembly (MEA) preparation.**—MEAs were prepared by the decal transfer method, using Vulcan carbon supported platinum catalysts (Pt/C), namely 4.8wt.% Pt/C (TEC10V50E, Tanaka, Japan) for the working electrode (WE) and 45.6wt.% Pt/C (TEC10V50E, Tanaka) for the counter electrode (CE). For the catalyst inks, a defined amount of catalyst was mixed with 1-propanol, ultrapure water, and ionomer solution (Asahi Kasei, Japan, 700 equivalent weight). The water concentration of the ink was 7wt.% (WE) or 16wt.% (CE), while the catalyst content was 0.02 (WE) or 0.04  $\text{g}_{\text{cat}} \text{ml}_{\text{ink}}^{-1}$  (CE), respectively. The ionomer/carbon (I/C) ratio was fixed to 0.65  $\text{g}_I \text{g}_C^{-1}$  for all electrodes. The inks were mixed by placing the bottles onto a roller mill at 60 rpm for 18 h at 25 °C. Then, the Mayer rod technique (coating machine: K Control Coater, RK PrintlCoat Instruments Ltd, England) with the appropriate bar size was used to achieve loadings of  $\approx 1.2\text{--}1.6 \mu\text{g}_{\text{Pt}} \text{cm}^{-2}_{\text{MEA}}$  (WE) and  $400 \pm 10 \mu\text{g}_{\text{Pt}} \text{cm}^{-2}_{\text{MEA}}$  (CE) on virgin PTFE decals. The unsymmetrical MEAs were fabricated by hotpressing the air dried decals onto a 12  $\mu\text{m}$  membrane (Asahi Kasei Corp., Japan) at 155 °C for 3 min with an applied pressure of 0.11  $\text{kN cm}^{-2}$ . The platinum loadings were determined by weighing the decals before and after the catalyst layer transfer using a high-precision balance (XPE105, METTLER TOLEDO, USA); owing to the rather small mass of the deposited catalyst layer for the  $\approx 1.2\text{--}1.6 \mu\text{g}_{\text{Pt}} \text{cm}^{-2}_{\text{MEA}}$  working electrode ( $\approx 0.21\text{--}0.27 \text{ mg}$  electrode coating for the  $5 \text{ cm}^2$  active area), the error for the quantification of the Pt loading of working electrode is estimated to be on the order of  $\pm 10\%$ . This, however, does not impact the precision of the determined exchange current densities, since these are referenced to the electrochemically active surface area (ECSA) obtained by CO stripping voltammetry (see below). The thickness of the working electrodes ranges between  $\approx 0.5\text{--}0.7 \mu\text{m}$ , based on the correlations given by Harzer et al.<sup>42</sup>

**$\text{H}_2$ -pump measurement procedure.**—In the  $\text{H}_2$ -pump experiments, the electrode with the very low Pt loadings ( $\approx 1.2\text{--}1.6 \mu\text{g}_{\text{Pt}} \text{cm}^{-2}_{\text{MEA}}$ ) served as working electrode, while the electrode with the high Pt loadings ( $\approx 400 \mu\text{g}_{\text{Pt}} \text{cm}^{-2}_{\text{MEA}}$ ) served both as counter electrode and as reference electrode (due to the high Pt loadings, the maximum overpotential of the working electrode at each pressure/temperature condition is estimated to be  $\approx 2 \text{ mV}$  at the highest current density). Thus, the working electrode potential is essentially at 0 V vs the reversible hydrogen electrode (RHE) potential at the given  $\text{H}_2$  partial pressure, with a maximum error of  $\approx 2 \text{ mV}$  at the highest current density. Prior to any kinetic measurements, each cell was conditioned to activate the catalyst. Due to the extremely low loading of the WE, a standard conditioning in an  $\text{H}_2$ /air setup did not lead to a stable performance. Instead, a voltage-controlled ramp-in procedure in a  $\text{H}_2/\text{H}_2$  setup (80 °C, 90% relative humidity (RH), flow rates of 2000/2000 nccm at a  $\text{H}_2$  partial pressure of 450/450  $\text{kPa}_{\text{H}_2}$ ) was used, polarizing the working electrode to the following potentials:  $+0.35 V_{\text{RHE}}$  for 20 min,  $+0.75 V_{\text{RHE}}$  for 5 min, 5 min at open circuit voltage (OCV),  $-0.2 V_{\text{RHE}}$  for 10 min, and finally again 5 min at OCV. This sequence was repeated 10 times until a constant performance was reached.

The HOR/HER kinetic measurements were then performed at each combination of temperature (30 °C, 40 °C, 60 °C, 80 °C, and 90 °C) and partial pressure of  $\text{H}_2$  (100 °C, 200 °C, 300 °C, and 450  $\text{kPa}_{\text{H}_2}$ ) in  $\text{H}_2/\text{H}_2$  (2000/2000 nccm) configuration at 90% RH (note that cell pressure is controlled to a value corresponding to the sum of the  $\text{H}_2$  partial pressure and the  $\text{H}_2\text{O}$  partial pressure calculated for 90% RH at a given temperature). At each condition, cyclic voltammograms (CVs) were recorded between  $-0.3 V_{\text{RHE}}$  and  $0.6 V_{\text{RHE}}$  at scan rates of  $100 \text{ mV s}^{-1}$  (20 cycles) and  $5 \text{ mV s}^{-1}$

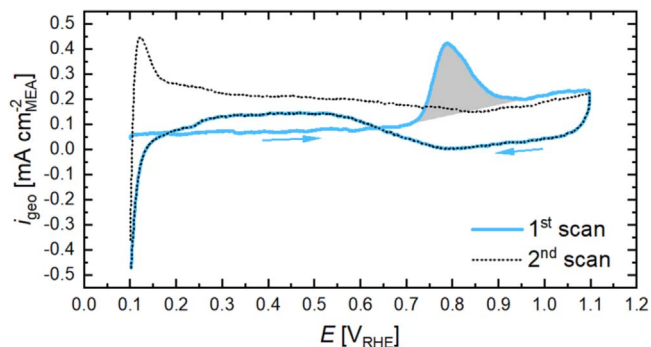


**Figure 1.** CO stripping voltammogram (blue solid line, arrows indicating the scan direction) and subsequent CV (black dotted line) of the Pt/C working electrode ( $1.4 \mu\text{g}_{\text{Pt}} \text{cm}_{\text{MEA}}^{-2}$ ) recorded after the HOR/HER kinetic measurements at a scan rate of  $50 \text{ mV s}^{-1}$  from 0.1 to 1.1  $V_{\text{RHE}}$  at 150  $\text{kPa}_{\text{abs}}$  and 40 °C (constant flows of 200  $\text{nccm}$  5%  $\text{H}_2/\text{Ar}$  on the CE and 5  $\text{nccm}$   $\text{N}_2$  on the WE). CO was adsorbed for 10 min at 0.1  $V_{\text{RHE}}$  at a flow of 10%  $\text{CO}/\text{N}_2$  (100  $\text{nccm}$ ) prior to the CV, followed by a 2 h purging procedure with  $\text{N}_2$  while maintaining the potential at 0.1  $V_{\text{RHE}}$ . To obtain the ECSA, the CO stripping current was integrated using a linear baseline (grey area) and converted to a corresponding Pt surface area using a specific capacity of  $420 \mu\text{C cm}_{\text{Pt}}^{-2}$ .

(3 cycles), followed by a galvanostatic electrochemical impedance spectroscopy (EIS) measurement at OCV with a  $2 \text{ mA cm}_{\text{MEA}}^{-2}$  AC current perturbation between 500 kHz and 1 Hz (10 points per decade) to determine the high frequency resistance (HFR; in  $\text{m}\Omega \text{cm}_{\text{MEA}}^{-2}$ ). The HFR was used to correct the  $\text{H}_2$ -pump cell potential ( $E_{\text{cell}}$ ) for the Ohmic drop in order to obtain the  $i\text{R}$ -free cell voltage ( $E_{i\text{R-free}}$ ) that corresponds to the working electrode potential on the RHE potential scale at the given  $\text{H}_2$  partial pressure:

$$E_{i\text{R-free}} = E_{\text{cell}} - i \cdot \text{HFR} \quad [6]$$

Here,  $i$  is the geometric current density (in  $\text{A cm}_{\text{MEA}}^{-2}$ ), which is positive for the HOR and negative for the HER on the working electrode. These potentiodynamic measurements were followed by a set of galvanostatic and potentiostatic measurements. For galvanostatic measurements, a DC current was drawn for 60 s and the resulting potential response was averaged over the last 10 s; this was followed by an EIS measurement at the same current, with a current amplitude of 10% of the DC current (from 500 kHz to 1 Hz, with 10 points per decade). These measurements were performed for currents between  $\pm 0.0117 \text{ A cm}_{\text{MEA}}^{-2}$  and  $\pm 0.074 \text{ A cm}_{\text{MEA}}^{-2}$  in ascending order (4 different DC current values) by alternating between anodic and the corresponding cathodic current in order to precisely determine the reversible potential at each condition.

Following these galvanostatic measurements, potentiostatic measurements were conducted in the analogous manner by applying a given potential for 60 s and averaging the resulting current during the last 10 s, followed by a potentiostatic EIS at the same potential using a potential amplitude of 1% of the DC potential (from 500 kHz to 1 Hz, with 10 points per decade). The potentiostatic testing was performed for potentials between  $\pm 5 \text{ mV}$  and  $\pm 450 \text{ mV}$  (cathodic potentials only until  $-200 \text{ mV}$ ) in ascending order and alternating between anodic and equal cathodic potentials. After each data point (static hold plus EIS), a relaxation step of 5 or 60 s (after potentials exceeding  $\pm 0.1 \text{ V}$ ) at OCV was implemented to ensure steady-state conditions for the next point. Due to the limitations of the potentiostat, data exceeding a total current of  $>30 \text{ A}$  (corresponding to  $>6 \text{ A cm}_{\text{MEA}}^{-2}$ ) could not be recorded.

All measurements were conducted for five MEAs. The HOR/HER curves were evaluated for each MEA and each condition individually before averaging the obtained values over all MEAs (error bars represent the standard derivation). Slopes represent an error-weighted fit of the averaged data.

### Surface area determination by CO stripping voltammetry.—

Due to the extremely low loadings, the voltammetric hydrogen under potential deposition ( $\text{H}_{\text{upd}}$ ) currents are severely overlapped by the onset of the HER and by hydrogen crossover induced HOR. Thus, the electrochemically active surface area (ECSA) was determined by CO stripping voltammetry that was performed after all kinetic measurements had been completed on a second G60 test station (Greenlight Innovation Corp., USA) to avoid CO poisoning during the  $\text{H}_2$ -pump measurements (see above). CO stripping was done according to a previously reported procedure<sup>42</sup> by adsorbing CO (using 10%  $\text{CO}$  in  $\text{N}_2$ , 100  $\text{nccm}$ ) for 10 min at 40 °C and 150  $\text{kPa}_{\text{abs}}$  while maintaining the cathode potential at 0.1  $V_{\text{RHE}}$  referenced to a nominal hydrogen partial pressure of 100  $\text{kPa}_{\text{abs}}$ . Subsequently, residual CO was removed from the cell and the gas lines by purging with nitrogen for  $\approx 2 \text{ h}$ . A CV from the CO adsorption potential to 1.1  $V_{\text{RHE}}$  at a scan rate of  $50 \text{ mV s}^{-1}$  was performed to oxidize the adsorbed CO. Two additional sweeps were recorded to verify the full oxidation and removal of CO from the electrode and the gas feed system. At the extremely low loadings used in this study, the hydrogen crossover current of  $\approx 0.18 \text{ mA cm}_{\text{MEA}}^{-2}$  severely distorts the CV shape, whereby the deactivation of the catalyst for the HOR occurs in the CO stripping region (above 0.7  $V_{\text{RHE}}$ ). Since CO poisoning prevents the oxidation of crossover hydrogen,<sup>37</sup> the conventional method of subtracting the subsequent CV as the baseline would lead to an underestimation of the ECSA due to HOR current being subtracted from CO oxidation current (overlapping grey area in Fig. 1). Instead, the ECSA was determined by integrating the area of the first anodic scan with a linear baseline rather than using a baseline based on the subsequent CV, using a specific charge of  $420 \mu\text{C cm}_{\text{Pt}}^{-2}$  (Fig. 1). The thus obtained Pt surface area of the low-loaded  $5 \text{ cm}^2$  active area electrodes falls within the range of  $7.0 \pm 1.5 \text{ cm}_{\text{Pt}}^2$ , corresponding to a so-called roughness factor ( $rf$ ) within the range of  $1.4 \pm 0.3 \text{ cm}_{\text{Pt}}^2 \text{ cm}_{\text{MEA}}^{-2}$ . Based on the Pt loading determined by weight measurements (ranging from 1.2–1.6  $\mu\text{g}_{\text{Pt}} \text{cm}_{\text{MEA}}^{-2}$ ) and the  $rf$  value for each of the working electrodes, the ECSA of the 4.8wt.% Pt/C catalyst of the WE equates to  $104 \pm 10 \text{ m}^2 \text{g}_{\text{Pt}}^{-1}$ ; this is in excellent agreement with the ECSA of  $104 \pm 1 \text{ m}^2 \text{g}_{\text{Pt}}^{-1}$  obtained for the same catalyst using electrodes with a higher and therefore more precisely quantifiable loading of  $15 \mu\text{g}_{\text{Pt}} \text{cm}_{\text{MEA}}^{-2}$ , validating the accuracy of the electrode weight measurements. In comparison, the roughness factor of the high-loaded counter electrodes is more than two orders of magnitude higher ( $\approx 240 \pm 30 \text{ cm}_{\text{Pt}}^2 \text{ cm}_{\text{MEA}}^{-2}$ ) compared to that of the low-loaded working electrodes.

## Results

### $\text{H}_2$ -pump measurements.—

In principle, kinetic data of electrochemical reactions can be determined either by potentiodynamic measurements, i.e., cyclic voltammetry (CV) or linear sweep voltammetry, or by steady-state measurements, i.e., potentiostatically or galvanostatically measured polarization curves. The former is most commonly done using RDE or micro-electrode measurements, where the effect of ohmic resistances and mass transport limitations is either constant throughout the measurement or very well defined. The latter is most commonly done using fuel cell measurements, where high current densities often lead to time dependent effects like membrane drying or pore flooding. For reactions with very fast kinetics like the HOR/HER on Pt, the mass transport resistance in the RDE configuration is generally too high to extract kinetic information from the data,<sup>4,15,16</sup> and the so-called  $\text{H}_2$ -pump configuration (a PEM fuel cell with  $\text{H}_2$  fed to both electrodes) in combination with ultra-low catalyst loadings on the working electrode has been used, as it offers 3–4 orders of magnitude faster mass transport rates compared to the RDE configuration.<sup>4,15</sup> In previous studies evaluating the HOR/HER kinetics of Pt based catalysts using the  $\text{H}_2$ -pump configuration or other measurement techniques that offer fast mass transport rates,

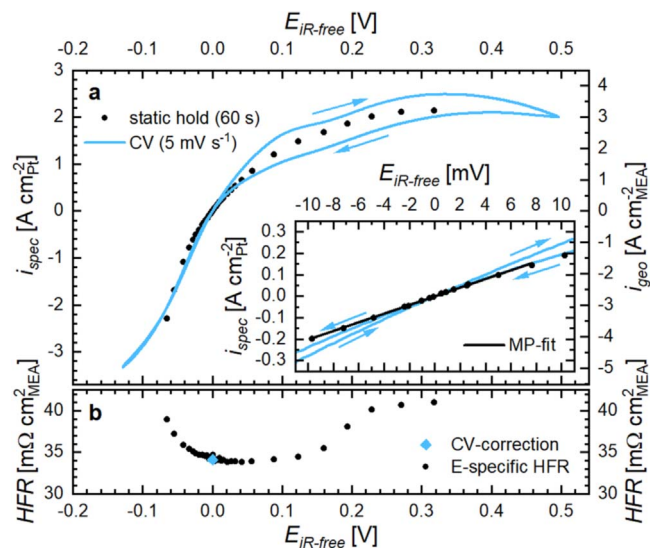


**Figure 2.** Representative hydrogen oxidation and evolution polarization curves on a Pt/C working electrode ( $1.4 \mu\text{g}_{\text{Pt}} \text{cm}_{\text{MEA}}^{-2}$ ;  $r_f = 1.5 \text{ cm}_{\text{Pt}}^2 \text{cm}_{\text{MEA}}^{-2}$ ) in a H<sub>2</sub>-pump configuration at 80 °C, 100 kPa<sub>H<sub>2</sub></sub>, 90% RH, and 2000/2000 nccm H<sub>2</sub>. (a) Specific current densities (left-hand y-axis) and geometric current densities (right-hand y-axis) vs  $E_{\text{IR-free}}$  (see Eq. 6) recorded by cyclic voltammetry at 5 mV s<sup>-1</sup> (blue solid lines) and by galvanostatic/potentiostatic measurements (black symbols, averaged over the last 10 s of a 60 s hold period), alternating between anodic and cathodic polarization (see Experimental section). The inset shows the micropolarization region ( $E_{\text{IR-free}} = \pm 10$  mV) and a corresponding linear fit for the galvanostatic/potentiostatic measurements according to Eq. 9. (b) Corresponding HFRs used for the iR-correction of the cell potential, recorded at OCV (i.e., at 0 V) for the CV based measurement (blue diamond) and at each data point for the galvanostatic/potentiostatic measurements (black circles). The Pt/C counter electrode Pt loading was  $\approx 400 \mu\text{g}_{\text{Pt}} \text{cm}_{\text{MEA}}^{-2}$ .

both the dynamic<sup>5,15,17,20,26</sup> and the steady-state approach<sup>4,21</sup> have been used. Here, both approaches have been examined, namely CVs recorded at 5 mV s<sup>-1</sup> as well as a combination of galvanostatic and potentiostatic measurements (Fig. 2).

As mentioned previously, the HOR/HER consists of a series of two of the three elementary steps shown in Eqs. 2–4. Thus, the possible reaction pathways are: (i) a Tafel-Volmer mechanism (TV), meaning a dissociative adsorption of hydrogen onto the platinum surface of the catalyst (Tafel reaction), followed by an electrochemical oxidation of the adsorbed hydrogen species (Volmer reaction); (ii) a Heyrovsky-Volmer mechanism (HV), meaning a partially oxidative adsorption of hydrogen (Heyrovsky reaction), again followed by the oxidation of the adsorbed hydrogen species (Volmer reaction); or, (iii) a combination of TV and HV. While a Tafel-Heyrovsky mechanism (TH) is conceivable, it has been argued to play no significant role.<sup>25</sup> The overall reaction rate for both the TV and the HV reaction sequences is generally assumed to follow a Butler-Volmer kinetics expression (see Eq. 5) at low HOR/HER overpotentials, i.e., close to the equilibrium potential.

Thus, an exponential relationship between the HOR/HER current density and overpotential for the anodic/cathodic branches at high overpotentials is expected. The potentiodynamic measurement (blue line in Fig. 2a), which was corrected for the HFR at OCV according to Eq. 6, clearly deviates from this behavior, as a distinct flattening of the current density vs overpotential curve could be observed at anodic/cathodic overpotentials exceeding an absolute value of  $\approx 50$  mV. On the anodic side, this flattening is much more pronounced than on the cathodic side, expressed by a rather constant limiting current plateau of  $\approx 3\text{--}4 \text{ A cm}^{-2}_{\text{MEA}}$  (see right-hand y-axis in Fig. 2) at high anodic overpotentials of  $\approx 250\text{--}500$  mV. The origin of this limiting current density could be ascribed to two different possible reasons: The first one would be a mass transport limitation

of the hydrogen reactant to the electrode, leading to a diffusion-limited current density, analogous to what is observed in RDE measurements.<sup>43</sup> However, in the here used H<sub>2</sub>-pump configuration recorded under differential-flow conditions (at  $4 \text{ A cm}^{-2}_{\text{MEA}}$ , the supplied H<sub>2</sub> flow of 2000 nccm corresponds to a  $\approx 14$ -fold H<sub>2</sub> excess) with a H<sub>2</sub> partial pressure of 100 kPa, the diffusion limited current density through the GDL and the electrode is at least an order of magnitude higher than the observed  $\approx 3\text{--}4 \text{ A cm}^{-2}_{\text{MEA}}$ . The second and at first glance more probable reason would then be a change of the rate determining step (RDS) in the HOR kinetics. This could, for example, be a switch of the RDS from a Volmer-step to either a Heyrovsky-step (in a HV mechanism) or a Tafel-step (in a TV mechanism). Considering that the current density seems to reach a rather potential-independent plateau at high anodic overpotentials,<sup>15</sup> it is more likely that here the Tafel-step becomes rate limiting (as proposed previously), as it is—other than the Heyrovsky-step—a completely potential independent adsorption process. The nature of this current limitation will be discussed in detail below.

In addition to the obvious current limitation in the HOR branch, the potentiodynamic data show a significant hysteresis between the anodic and cathodic scan direction. Although most obvious at high anodic overpotentials, this hysteresis can already be observed for small overpotentials in the micropolarization (MP) region, i.e., at small overpotentials between  $\pm 10$  mV (inset in Fig. 2a), resulting in slightly different slopes between the anodic-going and the cathodic-going scans. This hysteresis has already been reported in previous publications,<sup>5,15</sup> yet its origin is unclear. Due to the dependency on scan direction and scan rate (data not shown), the hysteresis is most likely caused by time and/or potential dependent effects, which could include significant dryout of the membrane over the course of the CV, differences in the local MEA temperature evolving at high current densities and high overpotentials (thus depending on the scan direction), and/or a hysteresis in anion adsorption or hydrogen coverage.<sup>5</sup>

In order to determine whether the observed difference between anodic and cathodic scans is a time dependent effect, the HOR/HER kinetics were also measured using steady-state polarization experiments. Here, a series of galvanostatic holds at low current densities (i.e., at low overpotentials) and potentiostatic holds at overpotentials of  $\geq +5$  mV or  $\leq -5$  mV were applied for 60 s hold periods (averaging the resulting potential or current over the last 10 s), whereby anodic and cathodic currents/potentials were applied in an alternating fashion (see Experimental section). This approach allowed for an equilibration of the potential/current response and of the local MEA temperature at any given current/potential and, more importantly, made it possible to determine the HFR at the end of each current/potential hold, thus resulting in a more accurate estimation of the actual HOR/HER overpotential ( $\eta$ ) via Eq. 7 (note that this is not possible for the above discussed potentiodynamic scans):

$$\eta = E_{\text{IR-free}}(E) = E_{\text{cell}} - i \cdot \text{HFR}(E) \quad [7]$$

The thus acquired current densities as well as the HFR vs  $\eta$  (i.e., vs  $E_{\text{IR-free}}$ ) are shown by the black circles in Figs. 2a and 2b, respectively. Note that previous studies have corrected the potential additionally for the effective proton sheet resistance ( $R_{\text{H}^+}^{\text{effective}}$ ; in  $\text{m}\Omega \text{ cm}_{\text{MEA}}^2$ ) via Eq. 8:<sup>4,15,44</sup>

$$R_{\text{H}^+}^{\text{effective}} = \frac{R_{\text{sheet}}}{3} = \frac{\delta_{\text{cl}}}{3 \cdot \sigma_{\text{H}^+} \cdot \varepsilon_i} \quad [8]$$

where the electrode's proton sheet resistance ( $R_{\text{sheet}}$ ) is estimated from the RH and temperature-dependent ionomer conductivity ( $\sigma_{\text{H}^+}$ , in  $\text{S cm}^{-1}$ ), the electrode's ionomer volume fraction ( $\varepsilon_i$ ), and the electrode thickness ( $\delta_{\text{cl}}$ , in cm). For the low-EW ionomer used in this study, with  $\sigma_{\text{H}^+} \approx 0.3 \text{ S cm}^{-1}$  at 80 °C and 100% RH,<sup>45</sup> an effective proton sheet resistance of only  $\approx 0.3 \text{ m}\Omega \text{ cm}_{\text{MEA}}^2$  is obtained for the

low-Pt-loaded working with a thickness of  $\approx 0.5 \mu\text{m}$  ( $\epsilon_1 = 0.2$ ).<sup>4</sup> Since this would result in an error of only  $\approx 2 \text{ mV}$  at the highest current densities and is much smaller than the observed variation in the HFR measurements, the contribution of  $R_{\text{H}^+}^{\text{effective}}$  was neglected in this study.

Regarding the current density vs overpotential response, the same current limitation of the HOR at high overpotentials could be observed for this galvanostatic/potentiostatic experiment (black symbols in Fig. 2a) as in the potentiodynamic experiments (blue line). While the galvanostatic/potentiostatic data followed the cathodic branch at least in the micropolarization region (see inset in Fig. 2a), they started to deviate for higher positive overpotentials, resulting in a current density vs overpotential response that lies in between the potentiodynamic response of for anodic and cathodic scans. Despite the alternating anodic/cathodic polarization in the galvanostatic/potentiostatic approach, a smooth current density vs overpotential response was obtained, suggesting that the hysteresis in the potentiodynamic measurements is most likely due to time dependent effects (i.e., due to insufficient equilibration time at each potential). While the HFR at 0 V is the same for both measurement approaches (see Fig. 2b), the HFR values acquired in the galvanostatic/potentiostatic experiments start to increase significantly at higher anodic/cathodic current densities or overpotentials, increasing by  $7 \text{ m}\Omega \text{ cm}_{\text{MEA}}^{-2}$  at an anodic overpotential of  $\approx 0.3 \text{ V}$ . This change in HFR is neglected when using the potentiodynamic measurement approach and, as a consequence, the HOR/HER overpotentials are overestimated in this case. The importance of this individual HFR correction at each current density becomes obvious when looking at the cathodic HER branch: while the potentiodynamic approach showed a distinct flattening of the current vs overpotential response that could be interpreted as a change in the RDS of the HER, this effect is not any more apparent for the galvanostatic/potentiostatic measurements with proper HFR correction. Thus, such inaccurate accounting of the HFR correction could lead to a misinterpretation of the reaction kinetics. Therefore, the galvanostatic/potentiostatic measurement procedure that allows for an equilibration of the reaction system and for a more precise HFR correction was chosen for the evaluation of the HOR/HER kinetics in this study.

The specific HOR/HER current densities of representative galvanostatic/potentiostatic measurements are depicted in the form of Tafel plots in Fig. 3 (upper panels) for different temperatures and pressures, whereby the overpotentials were determined from the

measured HFR values (lower panels) by means of Eq. 7. The Tafel plots in the upper panels of Fig. 3a ( $100 \text{ kPa}_{\text{H}_2}$ ) and Fig. 3b ( $450 \text{ kPa}_{\text{H}_2}$ ) show that the current density increases with increasing temperature due to faster reaction kinetics. Both the anodic and cathodic branches of the Tafel plots follow the Butler-Volmer equation at low overpotentials (lines in Fig. 3; the details of the fitting procedure are given below). In the HER branch, the kinetic data closely follow the Butler-Volmer fits over the entire measured potential interval, indicating that the associative desorption of hydrogen from the catalyst surface (Tafel reaction) is much faster than the proton reduction (Volmer reaction). On the other hand, the kinetic data in the HOR branch all exhibit the above discussed limiting current at high overpotentials (orange highlighted areas), which clearly increases with temperature and hydrogen partial pressure. Furthermore, the deviation of the kinetic data in the HOR branch from a simple Butler-Volmer relationship occurs already at rather low overpotentials, especially for low  $\text{H}_2$  partial pressures (see Fig. 3a). This is most apparent when comparing different partial pressures at the same temperature (Fig. 3c), where the HER currents increase only slightly with  $p_{\text{H}_2}$ , while the HOR currents increase significantly, thus leading to much more symmetrical Tafel plots at high  $\text{H}_2$  partial pressures. This gradual increase in HOR activity with hydrogen partial pressure correlates well with the assumption of a Tafel-limitation at high overpotentials: an increase in  $p_{\text{H}_2}$  leads to an increased rate of the Tafel reaction, resulting in a higher limiting current and delaying the change of the RDS from the potential-controlled Volmer reaction to the potential-independent Tafel reaction. The high asymmetry between the anodic and cathodic branches at small hydrogen partial pressures indicates that already at small overpotentials there is a significant effect of the apparently comparably slow dissociative hydrogen adsorption for the HOR, while the associative hydrogen desorption does not seem to limit the HER in the observed potential range.

As stated above, the HFR values were used to calculate the HOR/HER overpotentials (see Eq. 7), so that a variation of the HFR with the current density at any given operating conditions critically affects the kinetic analysis. While the HFR (bottom panels of Fig. 3) generally decreases for higher temperatures due to a higher proton conductivity of the membrane, an increase of the HFR is observed with higher overpotentials for all conditions. This HFR increase goes along with the higher current densities measured at higher overpotentials, so that it is more pronounced for

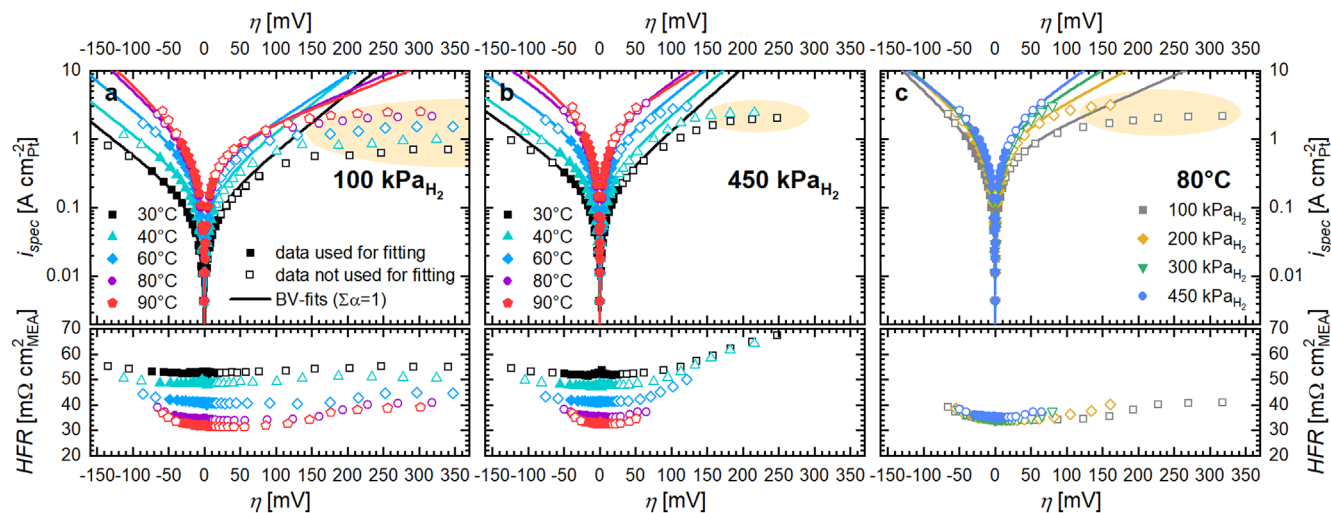


**Figure 3.** Kinetic current densities for the hydrogen oxidation and evolution reaction (top panels) and corresponding HFRs (bottom panels) of a representative MEA: temperature dependence at (a)  $100 \text{ kPa}_{\text{H}_2}$  and (b)  $450 \text{ kPa}_{\text{H}_2}$ , as well as (c)  $\text{H}_2$  partial pressure dependence at  $80^\circ\text{C}$  (all data at 90% RH and 2000/2000  $\text{ncm H}_2$ ). The data points used (filled symbols) and excluded (open symbols) for the shown Butler-Volmer fits (lines) represent the average over the last 10 s of a 60 s galvanostatic/potentiostatic hold period (see Experimental section). The selection criteria for data to be included in the Butler-Volmer fits are: (i) a less than  $1 \text{ m}\Omega \text{ cm}_{\text{MEA}}^{-2}$  HFR increase for the HER data; (ii) a current density of less than 10% of the limiting current density (orange shaded area) for the HOR data. Furthermore, the sum of the transfer coefficients in Eq. 5 was fixed to one (i.e.,  $\alpha_a + \alpha_c = 1$ ). The Pt/C working and counter electrode Pt loadings are  $1.4 \mu\text{g}_{\text{Pt}} \text{ cm}_{\text{MEA}}^{-2}$  and  $\approx 400 \mu\text{g}_{\text{Pt}} \text{ cm}_{\text{MEA}}^{-2}$ , respectively.

measurements at elevated temperatures and hydrogen partial pressures, as these resulted in higher current densities at a given overpotential. As the current density increases, the higher proton flux through the membrane leads to a higher water flux via electroosmotic drag, which in turn leads to a partial dry-out of the membrane that results in an increase of the HFR.<sup>46</sup>

**H<sub>2</sub>-pump data analysis.**—To obtain the kinetic parameters of the HOR/HER, the following kinetic analysis was performed individually for each tested MEA (five in total), and the extracted kinetic parameters for each MEA and test condition (exchange current densities, transfer coefficients, etc.) were then averaged, rather than fitting the averaged data points from all MEAs. This was considered more accurate, since differences between individual MEAs with regards to roughness factor or HFR can be accounted for easily and accurately in individual measurements, but would introduce uncertainties in overpotential when averaging over measurements with multiple MEAs.

The exchange current density  $i_0$  has been obtained by fitting the data using the Butler-Volmer equation (Eq. 5). To limit the effect of the HOR limiting current on the kinetic evaluation, only data points with a current density of less than 10% of the corresponding limiting current density were used for fitting; where the limiting current density could not be determined due to exceeding the current limitation of the potentiostat (30 A, corresponding to 5 A cm<sup>-2</sup>), the limiting current density was estimated using its dependence on the hydrogen partial pressure discussed in the last part of this work. Additionally, all data points with an HFR increase of more than 1 mΩ cm<sub>MEA</sub><sup>2</sup> compared to the average HFR within the range of ± 20 mV were excluded from the fit in order to ensure that the correction of the potential for the Ohmic drop was accurate under the relevant measurement conditions. Data points considered for a given Butler-Volmer fit are depicted as full symbols in Fig. 3, whereas data points that were excluded from the fit are depicted as open symbols. In order to obtain physically meaningful fits, the values of the anodic and cathodic transfer coefficients  $\alpha_a$  and  $\alpha_c$  of the Butler-Volmer equation need to be constrained in some way. For example, the sum of  $\alpha_a$  and  $\alpha_c$  can either be unity in the case of a Tafel-Volmer mechanism or a maximum of two in the case of a Heyrovsky-Volmer mechanism.<sup>28–30</sup> For the presented data, only fits with a sum of transfer coefficients of one ( $\alpha_a + \alpha_c = 1$ ) represented the data reasonably well, thus further confirming a predominant Tafel-Volmer mechanism. In previous publications by our group, the Butler-Volmer fitting of the HOR/HER kinetic data was furthermore limited to a symmetrical behavior, where both transfer coefficients were fixed to the value 0.5, assuming that both the anodic and cathodic parts of the reaction would behave symmetrical with regards to the overpotential.<sup>15,17</sup> To account for the obvious asymmetry in the Tafel-plots shown in Fig. 3, a higher degree of freedom with the sum of transfer coefficients only being fixed to one was chosen in this study, as this type of fitting represented the data much better even for data points that were excluded from fitting (see fitted curves in Fig. 3), and since we could not find a convincing explanation as to why the anodic and the cathodic branch of the reaction should be strictly symmetrical under all conditions. The obtained values for the exchange current densities are reported in Table I, while the anodic transfer coefficient are summarized in Fig. S1 (available online at [stacks.iop.org/JES/168/064516/mmedia](https://stacks.iop.org/JES/168/064516/mmedia)) in the SI, showing that the HOR/HER becomes more symmetrical at higher partial pressures of hydrogen and at lower temperatures, as  $\alpha_a$  approaches 0.5 under these conditions. To increase the comparability to other studies, all fits and data analysis were also performed using symmetrical transfer coefficients fixed to a value 0.5 (Figs. S2, S3 and S4).

Additionally, the micropolarization region (inset in Fig. 2) close to the HOR/HER equilibrium potential ( $\eta = \pm 10$  mV), where the overall influence of any mass transport limitations should be negligible, was fitted using the linearized form of the Butler-Volmer equation for

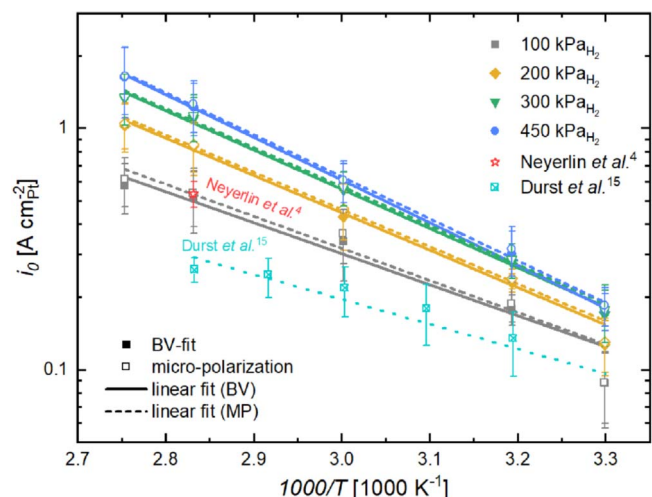


**Figure 4.** Pressure-dependent Arrhenius plots of the  $i_0$ -values of the HOR/HER on Pt/C determined in this work with the H<sub>2</sub>-pump setup and fitted from the BV-equation with the constraint  $\alpha_a + \alpha_c = 1$  (filled symbols and solid lines;  $i_0$ -values listed in Table I) and the micropolarization equation with the constraint  $\alpha_a + \alpha_c = 1$  (open symbols and dashed lines;  $i_0$ -values listed in Table SI) between 30 °C and 90 °C (averaged over five MEAs). The H<sub>2</sub>-pump based measurements at 100 kPa<sub>H2</sub> from Neyerlin et al.<sup>4</sup> (red open star) and from Durst et al.<sup>15</sup> (turquoise crossed squares; from BV-fitting with the constraint  $\alpha_a = \alpha_c = 0.5$ ) are given for comparison.

small overpotentials:<sup>28</sup>

$$i_0 \cdot (\alpha_a + \alpha_c) = \frac{R \cdot T}{F} \cdot \frac{i_{\text{spec}}}{\eta} \quad [9]$$

Here, the exchange current density can be obtained from the slope in the current-potential plots when the sum of transfer coefficients is known. For the reader's convenience, the obtained exchange current densities from the BV-fits with the constraints of either  $\alpha_a + \alpha_c = 1$  or  $\alpha_a = \alpha_c = 0.5$  as well as of the micropolarization (MP) fit with the constraint  $\alpha_a + \alpha_c = 1$  are compared in Table SI in the SI.

To investigate the temperature dependency of the HOR/HER, the apparent activation energy  $E_{A,\text{app}}$  (in kJ mol<sup>-1</sup>) of the exchange current density for any given H<sub>2</sub> partial pressure can be determined according to:

$$\left( \frac{\partial \log(i_0)}{\partial(1/T)} \right)_{p_{\text{H}_2}} = -\frac{E_{A,\text{app}}}{2.303 \cdot R} \quad [10]$$

Figure 4 shows the Arrhenius plots of  $i_0$  vs  $T^{-1}$  for different  $p_{\text{H}_2}$  values, either for the exchange current densities determined from the micropolarization region assuming  $\alpha_a + \alpha_c = 1$  (open symbols and dashed lines) or from the asymmetric Butler-Volmer fits with  $\alpha_a + \alpha_c = 1$  (filled symbols and solid lines). As could already be seen from comparing the  $i_0$ -values in Table SI, the difference in the differently deduced  $i_0$ -values is rather negligible. Both data sets follow straight lines in the Arrhenius plot and, within the experimental error, yield the same apparent activation energies (see Table I). In comparison to previous publications that determined the HOR/HER kinetics by the H<sub>2</sub>-pump approach, it can be seen that the here obtained  $i_0$  value at 80 °C and 100 kPa H<sub>2</sub> (red open star in Fig. 4) is essentially identical with that reported by Neyerlin et al.;<sup>4</sup> on the other hand, the exchange current densities between 40 °C–80 °C and 100 kPa H<sub>2</sub> reported by Durst et al.<sup>15</sup> (see turquoise crossed squares in Fig. 4) are ≈1.5–3 times lower and yielded a significantly lower activation energy of ≈16 kJ mol<sup>-1</sup> compared to the ≈25 kJ mol<sup>-1</sup> measured here. Interestingly, the former also used a static measurement approach (galvanostatically controlled in their

**Table I.** Pressure-dependent  $i_0$ -values obtained from the Butler-Volmer fits outlined in Fig. 3, averaged for five independently prepared and measured MEAs. The apparent activation energies ( $E_{A,app}$ ) were determined in the range of 30 °C to 90 °C (see Fig. 4) based on the  $i_0$ -values obtained either from Butler-Volmer fits ( $E_{A,app}$  (BV); Eq. 5) or from the micropolarization region ( $E_{A,app}$  (MP); Eq. 9), assuming in both cases a sum of transfer coefficients of one ( $\alpha_a + \alpha_c = 1$ ).

$p_{H_2}$ [kPa]	100	200	300	450
$i_0$ at 30 °C [ $A\ cm_{Pt}^{-2}$ ]	$0.088 \pm 0.031$	$0.13 \pm 0.03$	$0.17 \pm 0.04$	$0.18 \pm 0.03$
$i_0$ at 40 °C [ $A\ cm_{Pt}^{-2}$ ]	$0.18 \pm 0.03$	$0.23 \pm 0.02$	$0.28 \pm 0.04$	$0.30 \pm 0.07$
$i_0$ at 60 °C [ $A\ cm_{Pt}^{-2}$ ]	$0.34 \pm 0.11$	$0.43 \pm 0.12$	$0.55 \pm 0.10$	$0.59 \pm 0.12$
$i_0$ at 80 °C [ $A\ cm_{Pt}^{-2}$ ]	$0.52 \pm 0.15$	$0.84 \pm 0.20$	$1.10 \pm 0.24$	$1.23 \pm 0.30$
$i_0$ at 90 °C [ $A\ cm_{Pt}^{-2}$ ]	$0.58 \pm 0.14$	$1.03 \pm 0.23$	$1.33 \pm 0.33$	$1.63 \pm 0.53$
$E_{A,app}$ (BV) [ $kJ\ mol^{-1}$ ]	$24.6 \pm 2.8$	$29.6 \pm 1.8$	$31.1 \pm 1.1$	$33.9 \pm 1.0$
$E_{A,app}$ (MP) [ $kJ\ mol^{-1}$ ]	$25.4 \pm 3.3$	$29.5 \pm 1.8$	$30.9 \pm 1.0$	$33.3 \pm 1.1$

case) as performed in this study, whereas the latter used a potentiodynamic approach (at  $2\ mV\ s^{-1}$ ), which may (at part) be the reason for the lower exchange current densities and the lower apparent activation energy reported in the latter. However, the most striking observation from the Arrhenius plots in Fig. 4 is that the slope of the fitting lines increases with increasing hydrogen partial pressures, equating to an increase of the apparent activation energy from  $24.6 \pm 2.8\ kJ\ mol^{-1}$  at  $100\ kPa_{H_2}$  up to  $33.9 \pm 1.0\ kJ\ mol^{-1}$  at  $450\ kPa_{H_2}$  for the BV-fitting based data reported in Table I (this trend is only slightly smaller when based on the MP-fitting, with  $25.4 \pm 3.3\ kJ\ mol^{-1}$  at  $100\ kPa_{H_2}$  increasing to  $33.3 \pm 1.1\ kJ\ mol^{-1}$  at  $450\ kPa_{H_2}$ ). Thus, the HOR/HER kinetics exhibit an apparently non-constant activation energy, which increases gradually with hydrogen partial pressure.

## Discussion

In the following, we will more closely examine the possible origin of the  $H_2$  partial pressure dependence of the activation energy of  $i_0$  deduced from Fig. 4 and given in Table I, determine the reaction order of the HOR/HER kinetics with respect to  $H_2$  partial pressure, and discuss two different mechanisms that could lead to the observed limiting current for the HOR at high anodic overpotentials.

**$H_2$  partial pressure dependence of the activation energy.**—At first glance, the  $H_2$  partial pressure dependence of the activation energy of  $i_0$  (see Table I) at low anodic and cathodic overpotentials is surprising, since the rate determining Volmer reaction does not involve gaseous  $H_2$  and would thus be expected to be independent of  $p_{H_2}$ . However, when considering that the presumed rate determining Volmer reaction is preceded by a Tafel reaction that is in equilibrium, the effect of  $p_{H_2}$  on  $i_0$  can be rationalized. In this case, when describing the Tafel reaction by a dissociative Langmuir adsorption isotherm, an increase in  $H_2$  partial pressure at any given overpotential would be expected to result in an increase in the  $H_{ads}$  coverage, which in turn was found to somewhat lower the  $H_{ads}$  adsorption energy and bond strength;<sup>47–50</sup> for a Volmer rate determining step, the latter effect would be expected to lead to the observed increase of  $i_0$  with  $p_{H_2}$  (see Fig. 4).

An alternative view would be to consider the mechanistic analogy between a Tafel-Volmer mechanism and a “potential dependent” Langmuir-Hinshelwood mechanism with a dissociative adsorption step. The rate of the HOR,  $r_{HOR}(\eta, p_{H_2})$ , would then depend on the potential dependent rate constant of the Volmer reaction for the HOR,  $k_{HOR}(\eta)$ , and the potential dependent surface coverage,  $\theta_H(\eta, p_{H_2})$ :

$$r_{HOR}(\eta, p_{H_2}) = k_{HOR}(\eta) \cdot \theta_H(\eta, p_{H_2}) \quad [11]$$

While these dependencies cannot be determined from the here presented kinetic data, assuming a Langmuir-Hinshelwood mechanism might nevertheless help to understand the pressure dependency of the determined activation energies. At the HOR/HER

equilibrium potential, the Volmer-step has exactly the same absolute rate for the HER and the HOR, so that the  $H_{ads}$  surface coverage remains constant and is only controlled by the equilibrium coverage established through the Tafel reaction. As the overall reaction at 0 V vs RHE is not driven by potential (as  $\eta = 0$ ), a potential independent or classical Langmuir-Hinshelwood mechanism can be considered as a reasonable approximation. In this case, the adsorption enthalpy  $\Delta H_{ads}$  (marked in orange in Fig. 5) affects the measurable apparent activation energy  $E_{A,app}$  (marked in blue).<sup>51,52</sup> While the true activation energy of the Volmer reaction  $E_A$  (marked in black), i.e., the energy difference between the transition state and  $H_{ads}$ , is roughly constant (clearly only a first-order estimate, as discussed above), the effect of  $\Delta H_{ads}$  at the equilibrium potential ( $\eta = 0$ ) would depend on the surface coverage of  $H_{ads}$  ( $\theta_H$ ), which in turn is a function of the  $H_2$  partial pressure according to Eq. 12 (this corresponds to Eq. 126 in ref. 51) and Eq. 13 (adapted for Eq. 11 in this work according to eqs. 48–52 in ref. 51) with the equilibrium constant  $K$  in units of  $Pa^{-1}$ :

$$\theta_H(\eta = 0) = \frac{\sqrt{K \cdot p_{H_2}}}{1 + \sqrt{K \cdot p_{H_2}}} \quad [12]$$

$$\begin{aligned} E_{A,app}(\eta = 0) &= E_A + \Delta H_{ads} - \theta_H \cdot \Delta H_{ads} \\ &= E_A + \Delta H_{ads} \cdot (1 - \theta_H) \end{aligned} \quad [13]$$

As our experiments do not allow for a direct measure of the  $H_{ads}$  coverage during the HOR/HER, the apparent activation energy can only be determined as a function of  $H_2$  partial pressure. Since  $\Delta H_{ads}$  is a negative quantity and since  $\theta_H$  will increase with increasing  $p_{H_2}$ ,  $E_{A,app}$  is expected to increase with pressure, consistent with the values listed in Table I; eventually,  $E_{A,app}$  should approach the activation energy of the Volmer reaction ( $E_A$ ) at very high  $H_2$  partial pressures. In summary, the experimentally observed decrease of  $E_{A,app}$  with increasing  $p_{H_2}$  can at least be qualitatively rationalized by drawing an analogy to the Langmuir-Hinshelwood mechanism.

**Estimation of the reaction order with respect to hydrogen partial pressure.**—The increase in the apparent activation energy of  $i_0$  with  $p_{H_2}$  has unexpected implications on the HOR/HER kinetics with respect to  $H_2$  partial pressure. The exchange current density,  $i_0$ , is expected to depend on the hydrogen concentration  $c_{H_2}$  on the catalyst surface, i.e., on the  $H_2$  concentration in the ionomer phase that is considered to cover the Pt particles. Assuming Henry’s Law, the  $H_2$  concentration in the ionomer phase should be directly proportional to the hydrogen partial pressure  $p_{H_2}$ .<sup>28</sup>

$$\frac{i_0}{i_0^*} \propto \left( \frac{c_{H_2}}{c_{H_2}^*} \right)^m \propto \left( \frac{p_{H_2}}{p_{H_2}^*} \right)^m \quad [14]$$

Here,  $i_0^*$  stands for the exchange current density measured at a reference concentration  $c_{H_2}^*$ , e.g., the concentration obtained at the

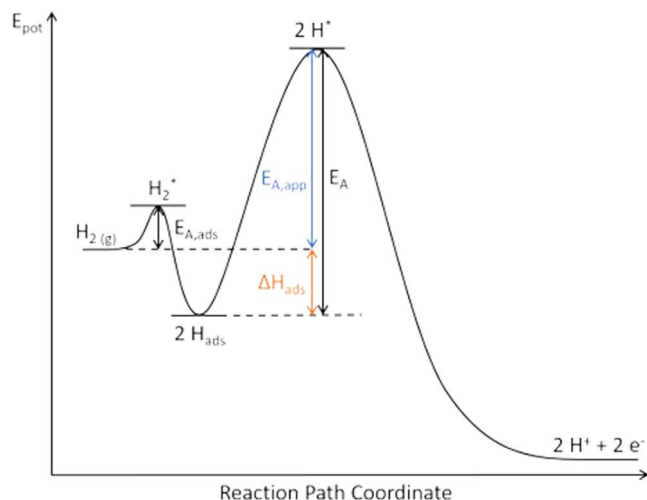


**Figure 5.** Scheme of the potential energy diagram for the catalytic oxidation of hydrogen with a dissociative adsorption of  $H_2$  (Tafel reaction) with the activation energy  $E_{A,ads}$  preceding the oxidation of  $H_{ads}$  (Volmer reaction) with its activation energy  $E_A$  being composed of the measurable apparent activation energy  $E_{A,app}$  (blue) and a surface coverage dependent contribution of the adsorption enthalpy  $\Delta H_{ads}$  (orange). Figure combined and adapted from *Concepts of Modern Catalysis and Kinetics*,<sup>51</sup> and *Fundamental Concepts in Heterogeneous Catalysis*.<sup>52</sup>

reference pressure of  $p_{H_2}^* = 100$  kPa. Thus, we can obtain the reaction order with respect to  $p_{H_2}$  (i.e.,  $m$ ) from the slope in the double logarithmic plot of  $i_0$  vs  $p_{H_2}$  at any given reaction temperature, which is shown in Fig. 6. As revealed by the values of these slopes marked in Fig. 6, the reaction order  $m$  also increases with temperature. This is a direct consequence of the increase in apparent activation energy with  $H_2$  partial pressure, as this results in a larger pressure induced spread in the  $i_0$ -values at higher temperatures. An exception to this here observed trend is the rather high slope of  $0.47 \pm 0.08$  for data recorded at 30 °C. At this temperature, the measured  $i_0$ -values for all pressures were lower than one would expect from the Arrhenius plot (Fig. 4), with the deviation being most severe for low pressures. This might be the result of operating at the limit of the test station's capabilities with respect to a tight control of both the cell temperature and the dewpoint (i.e., the humidification), due to the small difference between room temperature ( $\approx 25$  °C) and the set cell and dewpoint temperatures; furthermore, at this lowest  $H_2$  partial pressure of 100 kPa, the required total cell pressure of 104 kPa (considering a water vapor pressure of  $\approx 4$  kPa at 30 °C and 90% RH) is very close to the ambient pressure. That these difficulties are a likely problem for the measurements at 30 °C, particularly at 100 kPa  $H_2$ , is also reflected by the larger standard deviation between the five measurements at this condition.

**HOR limiting currents at high anodic overpotentials.**—As discussed above, the Butler-Volmer plots in Fig. 3 clearly show a limiting HOR current at high anodic overpotentials (orange marked areas). The cell temperature and  $H_2$  partial pressure dependent values of the limiting current densities referenced to the electrochemically active Pt surface area ( $i_{lim}$ ) were determined from the HOR/HER data at anodic overpotentials of at least 150 mV, using as a criterion that the increase in the current density with increasing overpotential remain below 10% (for the thus determined values see Table SII in the SI). Analogous limiting currents for the HOR have been observed in several other studies, and were mostly attributed to a limitation by the Tafel reaction,<sup>15,18,38</sup> while the only study that explicitly addressed this limiting current by Zalitis et al. concluded that it is most likely a limitation due to a rate limiting Heyrovsky reaction.<sup>5</sup> The latter can be excluded based on the data in the present study, since a rate limiting Heyrovsky reaction would result in a

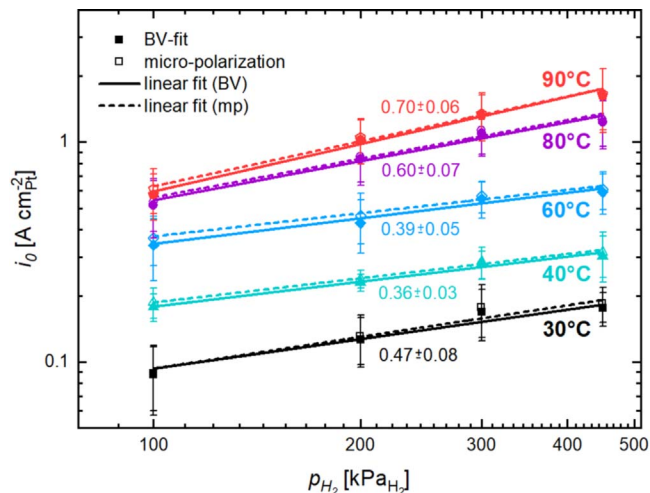


**Figure 6.** Double-logarithmic relation between the hydrogen partial pressure ( $p_{H_2}$ ) and the exchange current density ( $i_0$ ) estimated from the Butler-Volmer fits (filled symbols and solid lines, with the constraint  $\alpha_a + \alpha_c = 1$ ) or from the fits in the micropolarization region (open symbols and dashed lines, with the constraint  $\alpha_a + \alpha_c = 1$ ) at temperatures from 30 °C to 90 °C (averaged over five MEAs). The slopes represent the reaction order ( $m$ ) with respect to  $p_{H_2}$ , which are given by the numbers in the plot based on the  $i_0$ -values obtained from the BV-fits.

Tafel slope of 120 mV decade<sup>-1</sup>, whereas the hydrogen pump data shown in Fig. 3 reached a current density plateau that is independent of potential. Therefore, only two other possible causes can result in the observed limiting currents for the HOR: (i) the RDS being the dissociative adsorption of hydrogen, i.e., the Tafel reaction; and/or, (ii) a hydrogen mass transport limitation. With regards to the latter, at least bulk diffusion limitations through the diffusion medium and the electrode can be excluded for the here used  $H_2$ -pump experiments with ultra-thin working electrodes ( $\approx 0.5$ – $0.7$   $\mu$ m), ultra-low Pt roughness factors ( $1.4 \pm 0.3$   $cm_{Pt}^{-2}$   $cm_{MEA}^{-2}$ ), and with pure  $H_2$ : the bulk diffusion limited current densities in this case should be on the order of 50–100  $A$   $cm_{MEA}^{-2}$  (corresponding to at least  $\approx 30$ – $60$   $A$   $cm_{Pt}^{-2}$ ), and are thus at least an order of magnitude larger than the observed  $i_{lim}$ -values (see Table SII in the SI).

Thus, we will first focus on the kinetic investigation of an assumed rate limiting Tafel reaction at high anodic overpotentials. In this case, the H-adsorption rate of the Tafel reaction ( $r_{ads}$  in  $cm_{Pt}^{-2}$   $s^{-1}$ ) can be converted into a limiting current ( $i_{lim}(Tafel)$ , in units of  $A$   $cm_{Pt}^{-2}$ ) by means of the Faraday constant  $F$  (96484  $A$   $s$   $mol^{-1}$ ) and the Avogadro-constant  $N_A$  ( $6.022 \cdot 10^{23}$   $mol^{-1}$ ):

$$i_{lim}(Tafel) = \frac{r_{ads}}{N_A} \cdot F \quad [15]$$

According to kinetic gas and collision theory,  $r_{ads}$  can be described by Eq. 16:<sup>51</sup>

$$r_{ads} = N_0 \cdot \frac{d\theta_H}{dt} = S(T) \cdot \frac{2 \cdot p_{H_2} \cdot (1 - \theta_H)^2}{\sqrt{2 \cdot \pi \cdot m_{H_2} \cdot k_B \cdot T}} \quad [16]$$

Here,  $N_0$  is the active site density (in units of  $cm_{Pt}^{-2}$ ),  $S(T)$  is the sticking coefficient,  $m_{H_2}$  is the molecular mass of hydrogen (2.016 u),  $k_B$  is the Boltzmann-constant ( $1.381 \cdot 10^{-23}$   $J$   $K^{-1}$ ), and  $T$  is the temperature (in units of K). Furthermore, when the hydrogen adsorption at high anodic overpotentials is the rate determining step, one can assume that  $H_{ads}$  is instantaneously oxidized, so that the fraction of free adsorption sites ( $\theta_{\square}$ ) should be approximately one:

$$\theta_{\square} = 1 - \theta_H \approx 1 \quad [17]$$

Under these considerations, the rate of hydrogen adsorption is expected to be directly proportional to  $p_{H_2}$  according to Eq. 16,

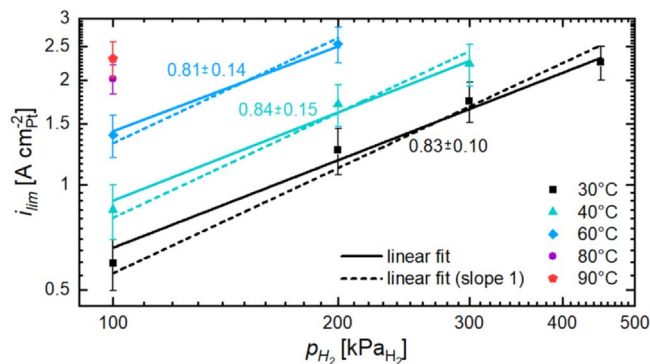


**Figure 7.** Double-logarithmic relationship between the hydrogen partial pressure ( $p_{\text{H}_2}$ ) and the limiting current density for the HOR at high anodic overpotentials ( $i_{\text{lim}}$ ), referenced to the electrochemically active Pt surface area and averaged over five independent measurements. The  $i_{\text{lim}}$ -values were obtained at anodic overpotentials of at least 150 mV, whereby data points for which the increase in current density to the next point exceeded 10% were excluded. The numerical values of the slopes determined by a linear fit (solid line, the slope represents the averaged slope obtained from five independently fitted measurements) are given in the figure and represent the reaction order with respect to  $p_{\text{H}_2}$ , while the dashed lines represent linear regression fits with a fixed slope of 1.0, i.e., assuming a direct proportionality between  $i_{\text{lim}}$  and  $p_{\text{H}_2}$ .

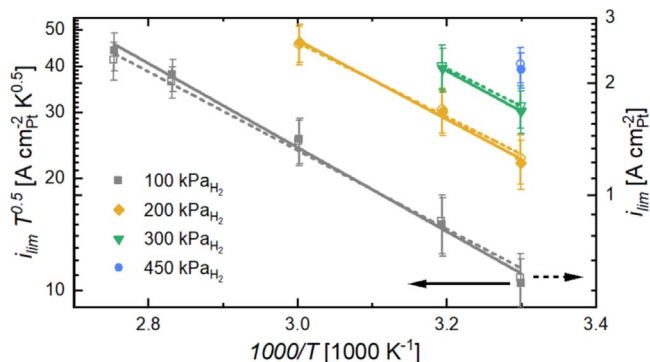


**Figure 8.** Arrhenius-type plots of the limiting HOR current density at high anodic overpotentials (from Table SII in the SI) with the temperature factor extracted from the pre-factor according to Eq. 19 ( $i_{\text{lim}} T^{0.5}$ , filled symbols and solid lines, left axis), assuming a dissociative Langmuir adsorption as the RDS; and of the limiting HOR current density directly ( $i_{\text{lim}}$ , open symbols and dashed lines, right axis).

which in turn implies that also the adsorption limited current density should be directly proportional to  $p_{\text{H}_2}$  (acc. to Eq. 15). Therefore, plotting the logarithm of the experimentally determined  $i_{\text{lim}}$ -values for the HOR (data in Table SII in the SI) vs the logarithm of  $p_{\text{H}_2}$  at a given temperature should result in straight lines with a slope of 1.0. This analysis is shown in Fig. 7 for the temperatures for which at least two limiting current density values could be determined (i.e., for 30 °C, 40 °C, and 60 °C), whereby the slopes of the linear regressions (solid lines) of 0.81–0.84 are slightly lower than the expected value of 1.0. However, since the linear fits with a fixed

slope of 1.0 (dashed lines) are still within the error range of the  $i_{\text{lim}}$  measurements (given by the vertical error bars that correspond to the standard deviation), it is reasonable to assume that  $i_{\text{lim}}$  for the HOR at high overpotentials is indeed directly proportional to  $p_{\text{H}_2}$  within the error of our measurements.

The temperature dependency of the Tafel reaction is more complex, as it not only involves the  $T^{-0.5}$  term from Eq. 16, but also the temperature dependence of the sticking coefficient  $S(T)$ . Embedded in the latter is the activation barrier for breaking the H-H-bond during the dissociative adsorption of  $\text{H}_2$ :<sup>51</sup>

$$S(T) = S_0 \cdot e^{-\frac{E_{\text{A,ads}}}{R \cdot T}} \quad [18]$$

Here,  $S_0$  ( $\leq 1$ ) is the pre-exponential factor of the sticking coefficient and  $E_{\text{A,ads}}$  is the activation energy of adsorption (see Fig. 5). Combining Eqs. 15–18 shows that  $E_{\text{A,ads}}$  can be determined directly from the slope of an Arrhenius-type plot of the limiting current density multiplied by  $T^{0.5}$ , as shown in Fig. 8 (filled symbols and solid lines). The thus determined activation energy of  $21 \pm 1 \text{ kJ mol}^{-1}$  is independent of the  $\text{H}_2$  partial pressure (see Table II), as expected for a dissociative adsorption step. This agrees well with an activation energy for the dissociative  $\text{H}_2$  adsorption on Pt of roughly  $17 \text{ kJ mol}^{-1}$  found in  $\text{H}_2$ - $\text{D}_2$  exchange experiments by Vogel et al.<sup>37</sup> These authors also reported an adsorption rate constant of  $k_{\text{ads}} \approx 2.4 \text{ cm s}^{-1}$  at 22 °C,<sup>37</sup> which would equate to a limiting current density of  $i_{\text{lim}} \approx 0.4 \text{ A cm}_{\text{Pt}}^{-2}$  at 100  $\text{kPa}_{\text{H}_2}$ , when assuming a hydrogen solubility of  $S_{\text{H}_2} \approx 8 \cdot 10^{-12} \text{ mol}_{\text{H}_2} \text{ cm}^{-3} \text{ Pa}^{-1}$  in the ionomer (from:  $i_{\text{lim}} = 2 \cdot F \cdot k_{\text{ads}} \cdot S_{\text{H}_2} \cdot p_{\text{H}_2}$ ).<sup>53</sup> This value is surprisingly close to the limiting current density of  $0.60 \pm 0.07 \text{ A cm}_{\text{Pt}}^{-2}$  at 30 °C obtained in the present study, supporting the idea that the Tafel reaction is responsible for the limiting HOR current density at high anodic overpotentials.

With these results providing strong support that the Tafel reaction is rate limiting the HOR at high anodic overpotentials, one nevertheless must reexamine the assumption that  $\text{H}_2$  mass transport limitations can indeed be ruled out (see Table II). As was already outlined above,  $\text{H}_2$  transport resistances through the diffusion medium and the electrode should be negligible, but the hydrogen transport resistance through the ionomer film covering the Pt particles might nevertheless be significant.<sup>54</sup> This film diffusion or local mass transport resistances are well known for  $\text{O}_2$  transport through the ionomer film in cathodes with low Pt loadings,<sup>55–58</sup> with any quantification being complicated by the likely inhomogeneous ionomer distribution and a presumably different morphology compared to bulk ionomer.<sup>59–61</sup> Still, the mass transport limited current density can be estimated using Fick's First Law that links the diffusive flux of  $\text{H}_2$  through the ionomer film ( $J_{\text{H}_2}$ , in  $\text{mol cm}^{-2} \text{ s}^{-1}$ ) to the diffusion coefficient ( $D_{\text{H}_2}$ , in  $\text{cm}^2 \text{ s}^{-1}$ ) and the  $\text{H}_2$  concentration gradient:<sup>51</sup>

$$J_{\text{H}_2} = -D_{\text{H}_2} \frac{dc}{dx} \quad [19]$$

The absolute value of the limiting current density is then obtained from the hydrogen maximum concentration gradient through an ionomer film of the thickness  $d_{\text{film}}$ , which occurs when the  $\text{H}_2$  concentration goes to zero at the ionomer/Pt interface, while at the

**Table II.** Pressure-dependent activation energies determined from the limiting HOR current densities at high anodic overpotentials. The values are deduced from the Arrhenius-type plots shown in Fig. 8, by two different methods, assuming two different mechanisms: (i) assuming a Tafel reaction RDS, plotting  $i_{\text{lim}} \cdot T^{0.5}$  vs  $1/T$  to obtain the activation energy for hydrogen adsorption ( $E_{\text{A,ads}}$ , see Fig. 5); (ii) assuming  $\text{H}_2$  mass transport resistance limitations through the ionomer film, plotting  $i_{\text{lim}}$  vs  $1/T$  to obtain the activation energy for  $\text{H}_2$  permeation ( $E_{\text{A,perm}}$ ). The data are averaged over 5 independent experiments.

$p_{\text{H}_2}$ [kPa]	100	200	300	450	Average
$E_{\text{A,ads}}$ [kJ mol <sup>-1</sup> ] ( $i_{\text{lim}} \cdot T^{0.5}$ )	$21.6 \pm 1.0$	$20.4 \pm 1.6$	$\approx 20.7$	—	$21 \pm 1$
$E_{\text{A,perm}}$ [kJ mol <sup>-1</sup> ] ( $i_{\text{lim}}$ )	$20.2 \pm 1.0$	$19.1 \pm 1.6$	$\approx 19.5$	—	$20 \pm 1$

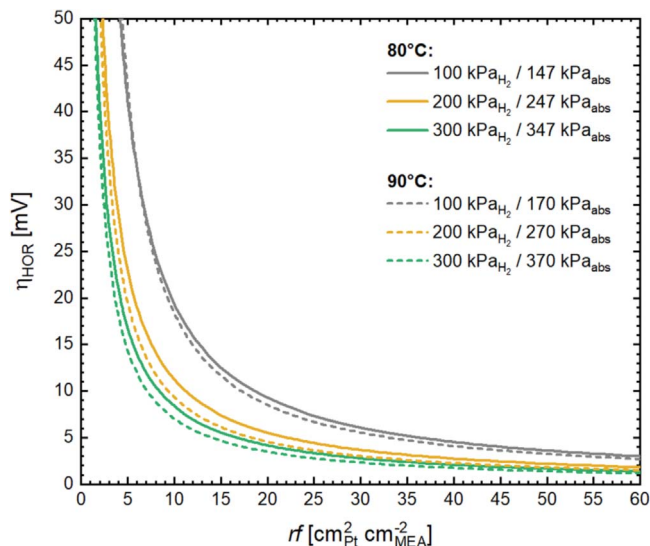


**Figure 9.** Kinetic HOR overpotential at  $3 \text{ A cm}_{\text{MEA}}^{-2}$  as a function of the anode roughness factor, calculated for  $80 \text{ }^{\circ}\text{C}$  and  $90 \text{ }^{\circ}\text{C}$  using the exchange current densities listed in Table I and the anodic transfer coefficients shown in Fig. S1. The absolute cell pressures (kPa<sub>abs</sub>) for operation at fully humidified conditions would be the sum of  $p_{\text{H}_2}$  and the water vapor saturation pressure at the respective temperature (47 kPa at  $80 \text{ }^{\circ}\text{C}$  and 70 kPa at  $90 \text{ }^{\circ}\text{C}$ ).

gas/ionomer interface it corresponds to the product of the hydrogen solubility in the ionomer ( $S_{\text{H}_2}$ , in  $\text{mol cm}^{-3} \text{ Pa}^{-1}$ ) and  $p_{\text{H}_2}$  in the gas phase, according to Henry's Law:

$$i_{\text{lim}}(\text{diff}) = 2 \cdot F \cdot J_{\text{H}_2} = 2 \cdot F \cdot D_{\text{H}_2} \frac{S_{\text{H}_2} \cdot p_{\text{H}_2}}{d_{\text{film}}} = 2 \cdot F \cdot \frac{p_{\text{H}_2} \cdot p_{\text{H}_2}}{d_{\text{film}}} \quad [20]$$

$$p_{\text{H}_2} = D_{\text{H}_2} \cdot S_{\text{H}_2} \quad [21]$$

In Eq. 20, the permeability of hydrogen through the ionomer ( $P_{\text{H}_2}$ ) is the product of the diffusion coefficient ( $D_{\text{H}_2}$ ) and the hydrogen solubility ( $S_{\text{H}_2}$ ), according to Eq. 21.<sup>53</sup>

The permeability of hydrogen at  $80 \text{ }^{\circ}\text{C}$  has been reported to range from  $\approx 10^{-16} \text{ mol cm}^{-1} \text{ s}^{-1} \text{ Pa}^{-1}$  for dry to  $\approx 3 \cdot 10^{-16} \text{ mol cm}^{-1} \text{ s}^{-1} \text{ Pa}^{-1}$  for fully humidified ionomer membranes,<sup>53,62</sup> which according to Eq. 20 would result in limiting current densities of  $\approx 6\text{--}19 \text{ A cm}_{\text{Pt}}^{-2}$  when assuming a film thickness of 3 nm (for an I/C ratio of  $0.65 \text{ g}_I \text{ g}_C^{-1}$ )<sup>45</sup> and  $100 \text{ kPa}_{\text{H}_2}$ ; the actual water content of the ionomer film might indeed be significantly lower than that expected for 90% RH, due to a possible ionomer dry-out that is indicated by the HFR increase at high anodic overpotentials (see Fig. 3). Similarly, for the same  $\text{H}_2$  partial pressure, temperature, and ionomer film thickness, a limiting current in the range of  $\approx 1.9 \text{ A cm}_{\text{Pt}}^{-2}$  can be calculated from a local mass transport resistance ( $R_{\text{T}}$ ) of  $\approx 350 \text{ s m}^{-1}$  reported by Schuler et al.,<sup>54</sup> using the correlation of  $R_{\text{T}}$  and  $i_{\text{lim}}$  established by Baker et al. (adapted from Eq. 3 for a two-electron oxidation of 100%  $\text{H}_2$ ):<sup>63</sup>

$$i_{\text{lim}}(\text{diff}) = \frac{2 \cdot F}{R_{\text{T}}} \cdot \frac{p_{\text{H}_2}}{R \cdot T} \quad [22]$$

As the ionomer film diffusion limited current densities ( $i_{\text{lim}}(\text{diff})$ ) estimated from the hydrogen permeability of a bulk membrane are only  $\approx 3\text{--}10$  times higher than the here measured limiting current density at  $80 \text{ }^{\circ}\text{C}$  and  $100 \text{ kPa H}_2$  ( $\approx 2.0 \text{ A cm}_{\text{Pt}}^{-2}$ ; see Table SII in the SI), and as the  $i_{\text{lim}}(\text{diff})$  estimate based on the actually measured local transport resistance yields a value that is essentially identical with the observed limiting current at high anodic overpotentials, it can unfortunately not be excluded that hydrogen mass transport

through the ionomer film might indeed affect or even govern the observed limiting HOR current at high anodic overpotentials.

One further option that we considered to distinguish whether the observed limiting currents can be ascribed to the Tafel reaction or to  $\text{H}_2$  mass transport through the ionomer film was to examine the temperature dependence of the latter. As shown in Eq. 20, the temperature dependence of the limiting current density is simply the temperature dependence of the  $\text{H}_2$  permeability, which for ionomeric membranes at a constant relative humidity is generally described by an Arrhenius-type law.<sup>62</sup> Thus, when limited by  $\text{H}_2$  mass transport through the ionomer film, plotting the logarithm of the limiting HOR current vs  $1/T$  should yield straight lines with a slope corresponding to  $-E_{\text{A,perm}}/R$ , where  $E_{\text{A,perm}}$  is the activation energy for  $\text{H}_2$  permeation through the ionomer phase and  $R$  is the gas constant. This is shown in Fig. 8 (open symbols and dashed lines, plotted vs the right-hand y-axis), yielding  $E_{\text{A,perm}} \approx 20 \pm 1 \text{ kJ mol}^{-1}$  when averaged over the data between  $100\text{--}300 \text{ kPa}_{\text{H}_2}$  (see Table II). This value is essentially identical with the activation energy for  $\text{H}_2$  permeation of  $E_{\text{A,perm}} \approx 19.7 \text{ kJ mol}^{-1}$  for  $\text{H}_2$  diffusion in Nafion at 95% RH,<sup>62</sup> and within the experimental error also the same as the activation energy for  $\text{H}_2$  adsorption ( $E_{\text{A,ads}}$ ) that was determined above when assuming a rate determining Tafel reaction (see Table II).

In summary, based on the above analysis, it is not possible to determine whether a rate limiting Tafel reaction or a  $\text{H}_2$  mass transport resistance through the ionomer film is responsible for the observed limiting HOR current density at high anodic overpotentials. One possible means to distinguish between these two phenomena would be to investigate the limiting HOR current density for different catalysts with different HOR/HER activities (e.g., platinum alloys<sup>26,64</sup>), or to examine electrodes with different I/C ratios that would result in different average ionomer film thicknesses.<sup>45</sup>

**Implications for low-loaded PEMFC anodes.**—In order to reach the current DoE target of  $125 \mu\text{g}_{\text{Pt}} \text{ cm}_{\text{MEA}}^{-2}$ ,<sup>65</sup> the state-of-the-art anode loadings of  $50 \mu\text{g}_{\text{Pt}} \text{ cm}_{\text{MEA}}^{-2}$  will likely have to be reduced to  $25 \mu\text{g}_{\text{Pt}} \text{ cm}_{\text{MEA}}^{-2}$  or even lower.<sup>66</sup> With a typical ECSA of  $\approx 60 \text{ m}^2 \text{ g}_{\text{Pt}}^{-1}$  for anode catalysts, this would correspond to an  $rf$  of 30 or  $15 \text{ cm}_{\text{Pt}}^2 \text{ cm}_{\text{MEA}}^{-2}$ , respectively, whereby ECSA losses of up to 50% due to SUS are expected over the MEA lifetime.<sup>9</sup> To correlate the here presented kinetic investigation of the HOR/HER to the expected contribution of the HOR to the overall cell performance on these low-loaded anodes, Fig. 9 shows the kinetic HOR overpotential as a function of the anode roughness factor, calculated via the Butler-Volmer equation (Eq. 5) for a current density of  $3 \text{ A cm}_{\text{MEA}}^{-2}$ , using the  $i_0$ -values reported in Table I and the  $\alpha_a$ -values shown in Fig. S1. For an  $rf$  of  $30 \text{ cm}_{\text{Pt}}^2 \text{ cm}_{\text{MEA}}^{-2}$ , minor HOR overpotentials of  $\approx 6 \text{ mV}$  are observed even at  $3 \text{ A cm}_{\text{MEA}}^{-2}$  at  $80 \text{ }^{\circ}\text{C}$  and  $100 \text{ kPa}_{\text{H}_2}$  (corresponding to a fully humidified cell pressure of  $147 \text{ kPa}_{\text{abs}}$ ). However, when the  $rf$  decreases to  $10 \text{ cm}_{\text{Pt}}^2 \text{ cm}_{\text{MEA}}^{-2}$  with lower anode loadings or after severe degradation, the HOR overpotential would increase to  $\approx 20 \text{ mV}$ . The analysis of Fig. 9 shows that for such a low  $rf$ , raising the  $\text{H}_2$  partial pressure to 200 or even  $300 \text{ kPa}_{\text{abs}}$  could significantly reduce the expected HOR overpotentials at  $80 \text{ }^{\circ}\text{C}$  to  $\approx 11$  or  $\approx 8 \text{ mV}$ , respectively, lowering the cell voltage loss by  $\approx 10 \text{ mV}$ ; Fig. 9 also shows that raising the cell temperature to  $90 \text{ }^{\circ}\text{C}$  has a diminishing effect on the performance of low-loaded anodes.

## Conclusions

In this study, a measurement procedure that allows for a precise determination of the HOR/HER kinetics over a broad range of temperatures, pressures, and overpotentials was developed. This approach combines galvanostatic/potentiostatic (a low/high overpotentials) hold periods of 60 s with impedance measurements, thereby allowing for a precise determination of the HFR at each measurement point and thus resulting in precise and reproducible kinetic data.

It could be shown that the HOR/HER follows a Tafel-Volmer mechanism in the observed range of temperatures and pressures. At low overpotentials, the rate determining Volmer-step is affected by the preceding Tafel-step, resulting in a significantly asymmetric behavior, with the symmetry increasing with higher partial pressures of hydrogen and lower temperatures (i.e., approaching equal anodic and cathodic transfer coefficients). Furthermore, a pressure dependence of the apparent activation energy of the Volmer-step was observed due to a pressure dependent contribution of the preceding Tafel-step's hydrogen adsorption enthalpy. The effect of the hydrogen adsorption enthalpy decreases with increasing surface coverage of adsorbed hydrogen, thus leading to an apparent increase of the measured activation energy with increasing hydrogen pressures. Due to this complex interaction between activation energy and hydrogen partial pressure, the reaction order of  $i_0$  with respect to  $p_{\text{H}_2}$  increases with temperature as well.

At high anodic overpotentials, the HOR approaches a limiting current that showed a direct proportionality to  $p_{\text{H}_2}$  and exhibited an apparent activation energy  $\approx 20 \text{ kJ mol}^{-1}$ . The origin of this limiting current could either be a change of the RDS to a rate limiting adsorption of  $\text{H}_2$  (rate limiting Tafel reaction) or a mass transport limitation of  $\text{H}_2$  through the ionomer film. Since both of these limitations would be expected to show the observed direct proportionality to  $p_{\text{H}_2}$ , as well as very similar apparent activation energies, it unfortunately could not be determined which of the two mechanisms is responsible for the limiting current at high anodic overpotentials.

### ORCID

Björn M. Stühmeier  <https://orcid.org/0000-0001-7713-2261>  
 Markus R. Pietsch  <https://orcid.org/0000-0003-3872-4496>  
 Jan N. Schwämmlein  <https://orcid.org/0000-0001-8902-4508>  
 Hubert A. Gasteiger  <https://orcid.org/0000-0001-8199-8703>

### References

1. K. Ayers, N. Danilovic, R. Ouimet, M. Carmo, B. Pivovar, and M. Bornstein, *Ann. Rev. Chem. Biomol. Eng.*, **10**, 219 (2019).
2. J. P. Torreglosa, P. García, L. M. Fernández, and F. Jurado, *Energy Convers. Manage.*, **77**, 514 (2014).
3. A. Chapman et al., *Int. J. Hydrogen Energy*, **44**, 6371 (2019).
4. K. C. Neyerlin, W. Gu, J. Jorne, and H. A. Gasteiger, *J. Electrochem. Soc.*, **154**, B631 (2007).
5. C. M. Zalitis, J. Sharman, E. Wright, and A. R. Kucernak, *Electrochim. Acta*, **176**, 763 (2015).
6. M. Bernt, A. Siebel, and H. A. Gasteiger, *J. Electrochem. Soc.*, **165**, F305 (2018).
7. H. A. Gasteiger, J. E. Panels, and S. G. Yan, *J. Power Sources*, **127**, 162 (2004).
8. W. R. Baumgartner, P. Parz, S. D. Fraser, E. Wallnöfer, and V. Hacker, *J. Power Sources*, **182**, 413 (2008).
9. J. N. Schwämmlein, P. J. Rheinländer, Y. Chen, K. T. Freyer, and H. A. Gasteiger, *J. Electrochem. Soc.*, **165**, F1312 (2018).
10. R. Borup et al., *Chem. Rev.*, **107**, 3904 (2007).
11. Y. Yu, H. Li, H. Wang, X.-Z. Yuan, G. Wang, and M. Pan, *J. Power Sources*, **205**, 10 (2012).
12. G. Couturier, D. W. Kirk, P. J. Hyde, and S. Srinivasan, *Electrochim. Acta*, **32**, 995 (1987).
13. P. J. Rheinländer, J. Herranz, J. Durst, and H. A. Gasteiger, *J. Electrochem. Soc.*, **161**, F1448 (2014).
14. J. Zheng, W. Sheng, Z. Zhuang, B. Xu, and Y. Yan, *Sci. Adv.*, **2**, e1501602 (2016).
15. J. Durst, C. Simon, F. Hasché, and H. A. Gasteiger, *J. Electrochem. Soc.*, **162**, F190 (2015).
16. W. Sheng, H. A. Gasteiger, and Y. Shao-Horn, *J. Electrochem. Soc.*, **157**, B1529 (2010).
17. J. Durst, A. Siebel, C. Simon, F. Hasche, J. Herranz, and H. A. Gasteiger, *Energy Environ. Sci.*, **7**, 2255 (2014).
18. M. Wesselmark, B. Wickman, C. Lagergren, and G. Lindbergh, *Electrochem. Commun.*, **12**, 1585 (2010).
19. H. Uchida, K. Izumi, K. Aoki, and M. Watanabe, *Phys. Chem. Chem. Phys.*, **11**, 1771 (2009).
20. C. M. Zalitis, A. R. Kucernak, J. Sharman, and E. Wright, *J. Mater. Chem. A*, **5**, 23328 (2017).
21. X. Wang, R. K. Ahluwalia, and A. J. Steinbach, *J. Electrochem. Soc.*, **160**, F251 (2013).
22. W. Sheng, Z. Zhuang, M. Gao, J. Zheng, J. G. Chen, and Y. Yan, *Nat. Commun.*, **6**, 5848 (2015).
23. J. Zheng, J. Nash, B. Xu, and Y. Yan, *J. Electrochem. Soc.*, **165**, H27 (2018).
24. H. A. Gasteiger, W. Gu, R. Makharia, M. F. Mathias, and B. Sompalli, "Handbook of fuel cells—fundamentals, technology and applications." ed. W. Vielstich, H. A. Gasteiger, A. Lamm, W. Vielstich, H. A. Gasteiger, and A. Lamms. *Fuel Cell Technology and Applications* (Wiley, Hoboken) p. 593 (2003).
25. A. R. Kucernak and C. Zalitis, *J. Phys. Chem. C*, **120**, 10721 (2016).
26. K. Elbert, J. Hu, Z. Ma, Y. Zhang, G. Chen, W. An, P. Liu, H. S. Isaacs, R. R. Adzic, and J. X. Wang, *ACS Catal.*, **5**, 6764 (2015).
27. J. N. Schwämmlein, B. M. Stühmeier, K. Wagenbauer, H. Dietz, V. Tileli, H. A. Gasteiger, and H. A. El-Sayed, *J. Electrochem. Soc.*, **165**, H229 (2018).
28. J. S. Newman, *Electrochemical systems* (Prentice Hall, Englewood Cliffs) (1991).
29. S. Fletcher, *J. Solid State Electrochem.*, **13**, 537 (2009).
30. R. Guidelli, G. Compton Richard, M. Feliu Juan, E. Gileadi, J. Lipkowski, W. Schmickler, and S. Trasatti, *Pure Appl. Chem.*, **86**, 245 (2014).
31. M. R. Gennero de Chialvo and A. C. Chialvo, *Phys. Chem. Chem. Phys.*, **6**, 4009 (2004).
32. E. Skúlason, V. Tripkovic, M. E. Björketun, S. Gudmundsdóttir, G. Karlberg, J. Rossmeisl, T. Bligaard, H. Jónsson, and J. K. Nørskov, *J. Phys. Chem. C*, **114**, 18182 (2010).
33. J. A. Santana, J. J. Saavedra-Arias, and Y. Ishikawa, *Electrocatalysis*, **6**, 534 (2015).
34. N. M. Marković, B. N. Grgur, and P. N. Ross, *J. Phys. Chem. B*, **101**, 5405 (1997).
35. B. E. Conway and G. Jerkiewicz, *Electrochim. Acta*, **45**, 4075 (2000).
36. J. Greeley, T. F. Jaramillo, J. Bonde, I. Chorkendorff, and J. K. Nørskov, *Nat. Mater.*, **5**, 909 (2006).
37. W. Vogel, L. Lundquist, P. Ross, and P. Stonehart, *Electrochim. Acta*, **20**, 79 (1975).
38. C. Jackson, G. T. Smith, M. Markiewicz, D. W. Inwood, A. S. Leach, P. S. Whalley, A. R. Kucernak, A. E. Russell, D. Kramer, and P. B. J. Levecque, *J. Electroanal. Chem.*, **819**, 163 (2018).
39. J. X. Wang, T. E. Springer, and R. R. Adzic, *J. Electrochem. Soc.*, **153**, A1732 (2006).
40. C. Simon, F. Hasché, D. Müller, and H. A. Gasteiger, *ECs Trans.*, **69**, 1293 (2015).
41. C. Simon, F. Hasché, and H. A. Gasteiger, *J. Electrochem. Soc.*, **164**, F591 (2017).
42. G. S. Harzer, J. N. Schwämmlein, A. M. Damjanović, S. Ghosh, and H. A. Gasteiger, *J. Electrochem. Soc.*, **165**, F3118 (2018).
43. T. J. Schmidt, H. A. Gasteiger, G. D. Stäb, P. M. Urban, D. M. Kolb, and R. J. Behm, *J. Electrochem. Soc.*, **145**, 2354 (1998).
44. K. C. Neyerlin, W. Gu, J. Jorne, A. Clark, and H. A. Gasteiger, *J. Electrochem. Soc.*, **154**, B279 (2007).
45. A. Orfanidi, P. Madkikar, H. A. El-Sayed, G. S. Harzer, T. Kratky, and H. A. Gasteiger, *J. Electrochem. Soc.*, **164**, F418 (2017).
46. W.-M. Yan, F. Chen, H.-Y. Wu, C.-Y. Soong, and H.-S. Chu, *J. Power Sources*, **129**, 127 (2004).
47. B. W. J. Chen and M. Mavrikakis, *Catalysis Science & Technology*, **10**, 671 (2020).
48. K. Christmann, G. Ertl, and T. Pignet, *Surf. Sci.*, **54**, 365 (1976).
49. L. Xu, Y. Ma, Y. Zhang, B. Teng, Z. Jiang, and W. Huang, *Science China Chemistry*, **54**, 745 (2011).
50. F. G. Will, *J. Electrochem. Soc.*, **112**, 451 (1965).
51. I. Chorkendorff and J. W. Niemantsverdriet, *Concepts of Modern Catalysis and Kinetics* (Wiley, Weinheim) (2003).
52. J. K. Nørskov, F. Studt, F. Abild-Pedersen, and T. Bligaard, *Fundamental Concepts in Heterogeneous Catalysis* (Wiley, Hoboken) (2014).
53. H. Ito, T. Maeda, A. Nakano, and H. Takenaka, *Int. J. Hydrogen Energy*, **36**, 10527 (2011).
54. T. Schuler, A. Chowdhury, A. T. Freiberg, B. Sneed, F. B. Spingler, M. C. Tucker, K. L. More, C. J. Radke, and A. Z. Weber, *J. Electrochem. Soc.*, **166**, F3020 (2019).
55. W. Yoon and A. Z. Weber, *J. Electrochem. Soc.*, **158**, B1007 (2011).
56. T. Suzuki, K. Kudo, and Y. Morimoto, *J. Power Sources*, **222**, 379 (2013).
57. G. S. Harzer, A. Orfanidi, H. El-Sayed, P. Madkikar, and H. A. Gasteiger, *J. Electrochem. Soc.*, **165**, F770 (2018).
58. J. P. Owejan, J. E. Owejan, and W. Gu, *J. Electrochem. Soc.*, **160**, F824 (2013).
59. F. C. Cetinbas, R. K. Ahluwalia, N. Kariuki, V. De Andrade, D. Fongalland, L. Smith, J. Sharman, P. Ferreira, S. Rasouli, and D. J. Myers, *J. Power Sources*, **344**, 62 (2017).
60. K. Karan, *Curr. Opin. Electrochem.*, **5**, 27 (2017).
61. S. A. Eastman, S. Kim, K. A. Page, B. W. Rowe, S. Kang, C. L. Soles, and K. G. Yager, *Macromolecules*, **45**, 7920 (2012).
62. C. K. Mittelsteadt and H. Liu, "Handbook of fuel cells—fundamentals, technology and applications." ed. W. Vielstich, H. A. Gasteiger, H. Yokokawa, W. Vielstich, H. A. Gasteiger, and H. Yokokawa. *Advances in Electrocatalysis, Materials, Diagnostics and Durability* (Wiley, Hoboken) p. 345 (2009).
63. D. R. Baker, D. A. Caulk, K. C. Neyerlin, and M. W. Murphy, *J. Electrochem. Soc.*, **156**, B991 (2009).
64. G. Shi, H. Yano, D. A. Tryk, A. Iiyama, and H. Uchida, *ACS Catal.*, **7**, 267 (2017).
65. U.S. Department of Energy, "Fuel Cell Technologies Program Multi-Year Research, Development, and Demonstration Plan" by the U.S. Department of Energy (2012), <https://energy.gov/eere/fuelcells/downloads/hydrogen-and-fuel-cell-technologies-office-multi-year-research-development>.
66. A. Kongkanand and M. F. Mathias, *J. Phys. Chem. Lett.*, **7**, 1127 (2016).